

# Optical vortex coronagraphy from soft spin-orbit masks

Artur Aleksanyan and Etienne Brasselet\*

*Univ. Bordeaux, LOMA, UMR 5798, F-33400 Talence, France*

*CNRS, LOMA, UMR 5798, F-33400 Talence, France and*

*Corresponding author: etienne.brasselet@u-bordeaux.fr*

We report on a soft route towards optical vortex coronagraphy based on self-engineered electrically tunable vortex masks based on liquid crystal topological defects. These results suggest that a Nature-assisted technological approach to the fabrication of complex phase masks could be useful in optical imaging whenever optical phase singularities are at play.

Observation of faint objects nearby a bright source of light is a basic challenge of high-contrast imaging techniques such as the quest for extrasolar planets in astronomical imaging, whose first observation dates two decades ago [1]. This has led to the development of instruments called coronagraphs, which combine high extinction of stellar light and high transmission of low-level signal at small angular separation. Stellar coronagraphy was initiated more than 80 years ago when Lyot studied solar corona without an eclipse by selective occultation of sunlight, placing an opaque disk in the focal plane of a telescope [2]. On the other hand, phase mask coronagraphs offer good performance for the observation of point-like sources. An early version consisted to use a disk  $\pi$ -phase mask [3] whose chromatic drawback arising from discrete radial phase step has been solved a few years later by incorporating discrete radial [4] or azimuthal [5] phase modulation to the original design. Later on, the proposed use of continuous azimuthal phase ramps improved the approach [6, 7] and led to the advent of optical vortex coronagraphy.

Vortex coronagraphs rely on the selective peripheral redistribution of on-axis light outside an area of null intensity at the exit pupil plane of the instrument, which is done by placing a spiraling phase mask in the Fourier plane characterized by a complex transmittance of the form  $\exp(i\ell\phi)$ , where the charge  $\ell$  is an even integer and  $\phi$  the usual azimuthal angle in the transverse plane. Indeed, this enables optimal on-axis rejection of light by placing an iris, often called Lyot stop, at the exit pupil plane while off-axis weak signal is almost unaffected for angular separation larger than the diffraction limit [8]. There are two families of optical vortex phase masks that respectively rely on scalar (phase) and vectorial (polarization degree of freedom) properties of light. The former case refers to straightforward helical shaping of the wavefront from a refractive phase mask whereas the latter one exploits the polarization properties of space-variant birefringent optical elements. Indeed, inhomogeneous anisotropic phase masks endowed with azimuthal optical axis orientation of the form  $\psi(\phi) = m\phi$  with  $m$  half-integer and associated with half-wave birefringent phase retardation leads to vortex mask of charge  $\ell = 2\sigma m$  for incident on-axis circularly polarized light beam with helicity  $\sigma = \pm 1$ , as originally shown in [9] using form birefringence (subwavelength grating of dielectric materials)

and in [10] using true birefringence (patterning of the orientation of a liquid crystal film).

The achromatic features of the vectorial option versus its scalar counterpart [11, 12] has eventually led to equip state-of-the-art large instruments such as Keck, Subaru, Hale, Large Binocular Telescope and Very Large Telescope with vectorial vortex coronagraphs. In practice, all these installations exploit vortex masks obtained either from brute-force nanofabrication, where form-birefringence arises from subwavelength material structuring [9], or liquid crystal polymers technology, where true birefringence is patterned on-demand [13]. Still, these high-tech ‘writing’ processes ultimately suffer from fabrication constraints and finite resolution preventing the creation of ideal material singularity, which implies various trade-off. One can mention the preferential use of natural rather than form-birefringence option at shorter wavelengths [11] and the use of an opaque disk to reduce the detrimental influence of central misorientation of the engineered optical axis pattern [14, 15]. The realization of higher-order masks generating optical phase singularities with even topological charges  $\ell > 2$  [6] that are desirable for future extremely large telescopes [16] is another manufacturing challenge. Since the basic technological bottle-neck can be identified as the man-made technology itself, a Nature-assisted approach would likely open a novel generation of vortex masks for optical vortex coronagraphy, which is the purpose of this work.

In fact, various kinds of spontaneously formed nematic liquid crystal topological defects have been previously demonstrated to behave as natural [17, 18] or field-induced [19–21] vectorial optical vortex generators with even charge  $|\ell| = 2$ . Optical vortex masks realized without need from machining technique have also been obtained from other mesophases such as cholesteric [22] and smectic [23] liquid crystals. Here we propose to explore the potential of self-engineered liquid crystals vortex phase masks for high-contrast imaging applications, in the particular case of optical vortex coronagraphy.

We choose so-called umbilical defects that appear in nematic liquid crystal films with perpendicular molecular alignment and negative dielectric anisotropy under quasi-static electric field and above a threshold voltage  $U = U^*$  of a few Volts [24]. These defects are associated with optical axis orientation angle of the form  $\psi(\phi) = m\phi + \psi_0$  with  $m = \pm 1$  and  $\psi_0$  a constant, see Figs. 1(a) and 1(b)

for typical polarized imaging, see later for experimental details. It has been shown previously that such defects behave as spin-orbit optical vortex generators [20]. This can be described by neglecting the diffraction inside the optical element itself given the circularly polarized incident field in the plane of the sample,  $E(r) \mathbf{c}_\sigma$ , where  $r = 0$  refers to the defect location and  $\mathbf{c}_\sigma = (\mathbf{x} + i\sigma\mathbf{y})/\sqrt{2}$  refers to circular polarization basis. In the case of transparent media as is our case, the output light field can be expressed as [25]

$$\mathbf{E}_{\text{out}}(r, \phi) \propto E(r) \exp[i\Delta(r)/2] \left\{ \cos[\Delta(r)/2] \mathbf{c}_\sigma + i \sin[\Delta(r)/2] \exp[i2\sigma\psi(\phi)] \mathbf{c}_{-\sigma} \right\}, \quad (1)$$

where  $\Delta(r)$  is the  $r$ -dependent birefringent phase retardation modeled following the work of Rapini [24]. Within such a description one has  $\Delta(r) = \delta(r/r_c)\Delta_\infty$ , where  $r_c = (L/\pi)(\mathcal{K}/K_3)^{1/2}[(U/U^*)^2 - 1]^{-1/2}$  is the voltage-dependent defect core radius with  $L$  the nematic film thickness,  $\mathcal{K} = K_2$  for  $m = +1$  and  $\psi_0 = \pi/2$  (our case) and  $\mathcal{K} = (K_1 + K_2)/2$  for  $m = -1$  whatever  $\psi_0$ , with  $K_{i=1,2,3}$  the Frank elastic constant of splay, twist and bend director distortions [26], and  $\Delta_\infty$  is the voltage-dependent asymptotic value of  $\Delta$  at large  $r$ . Calculated universal function  $\delta(r/r_c)$  and reduced core radius  $r_c/L$  versus reduced voltage  $U/U^*$  are shown in Figs. 1(c) and 1(d).

From Eq. (1), the spin-orbit generation of a spiraling optical phase with charge  $\pm 2$  for the helicity-flipped output field component is never ideally 100% pure due to the space-variant retardance, which is quantitatively evaluated by the purity

$$\eta = \int_0^\infty |E(r)|^2 \sin^2[\Delta(r)/2] r dr / \int_0^\infty |E(r)|^2 r dr, \quad (2)$$

$0 < \eta < 1$ , while the spin-orbit mask is described up to an unimportant phase factor by the complex amplitude

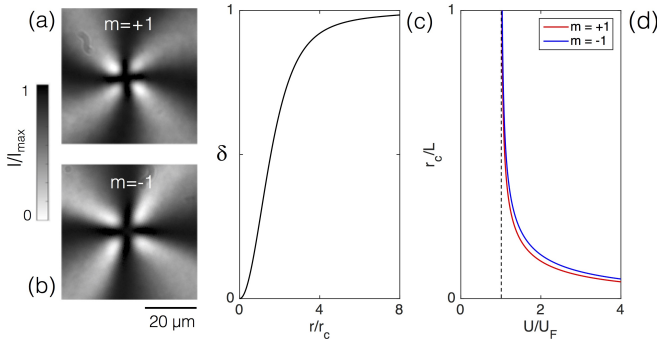


FIG. 1: (a,b) Typical images of nematic umbilical defects with topological charge  $m = \pm 1$  observed between crossed linear polarizers. (c) Calculated radial dependence of the universal function  $\delta$  from Rapini's model. (d) Calculated reduced core radius  $r_c/L$  versus reduced voltage  $U/U_F$  for  $m = +1$  (red curve) and  $m = -1$  (blue curve).

transmittance

$$\tau(r, \phi) = \sin[\Delta(r)/2] \exp[i\Delta(r)/2 + 2i\sigma\psi(\phi)]. \quad (3)$$

Looking for a complex transmittance of the form  $\exp(i\ell\phi)$  one should ideally target an umbilic with  $\Delta_\infty = \pi$  (that defines the voltage  $U = U_\pi$ ) and core radius  $r_c$  smaller enough than the characteristic beam spot size  $w$  in the plane of the sample. Here we choose a  $L = 10 \mu\text{m}$ -thick nematic film made from glass cell (from EHC Ltd) whose inner surface are provided with transparent indium-tin oxide electrodes. The liquid crystal film is prepared from the nematic MLC-2079 (from Li-crystal) having dielectric relative permittivity  $\varepsilon_\parallel = 4.1$  along the molecular alignment and  $\varepsilon_\perp = 10.2$  perpendicular to it (tabulated data at 1 kHz frequency) and refractive indices  $n_\parallel = 1.64$  and  $n_\perp = 1.49$  at 589 nm wavelength. The Frank elastic constant of splay, twist and bend director distortions [26] are  $K_1 = 15.9 \text{ pN}$  (tabulated),  $K_2 = 9.5 \text{ pN}$  (measured) and  $K_3 = 18.3 \text{ pN}$  (tabulated), respectively. This gives  $U^* = 1.83 \text{ V}_{\text{rms}}$ ,  $U_\pi = 2.52 \text{ V}_{\text{rms}}$  whatever  $m$  [24] and  $r_c = (2.4, 2.8) \mu\text{m}$  for  $m = \pm 1$ .

In practice, once  $U$  is set above  $U^*$ , a few defects remain at fixed location in the sample after the annihilation dynamics between nearby topological defects with opposite topological charges has taken place. Typically experiments are performed a couple of hours or more after the voltage has been switched on, whose steady value is set at  $U_\pi$ . Then, a defect is placed on-axis in the focal plane ( $P_F$ ) of a telescope as depicted in Fig. 2(a) that sketches the main part of the optical arrangement used to simulate a vortex coronagraph in the laboratory where starlight is mimicked by on-axis incident quasi-plane wave. Experiments are performed using point-like sources generated from He-Ne lasers at wavelength  $\lambda = 633 \text{ nm}$  and located in the focal plane of microscope objectives ( $10\times$ ,  $\text{NA} = 0.25$ ) with overfilled entrance pupil. Obtained light beams are collimated by lenses with 20 cm

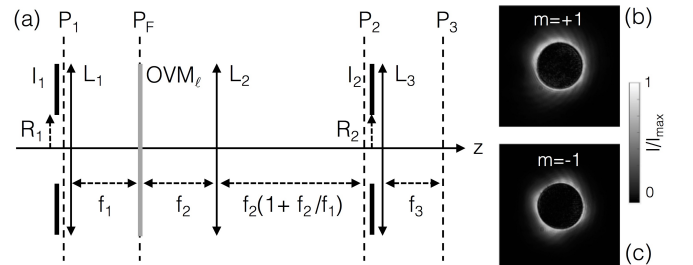


FIG. 2: (a) General description of the optical vortex coronagraph arrangement. It consists of a set of iris  $I_{1,2}$  and lenses  $L_{1,2,3}$  with focal lengths  $f_{1,2,3}$ , and an optical vortex mask of topological charge  $\ell$ ,  $\text{OVM}_\ell$ , placed in the Fourier plane  $P_F$  of the telescope formed by lenses  $L_{1,2}$ . The various planes of interest are labeled  $P_{1,F,2,3}$ . (b,c) Rings of fire observed in the exit pupil plane  $P_2$  for  $m = \pm 1$ .

focal length, apertured an iris with 25 mm diameter and remotely redirected at an angle  $\alpha$  from the optical axis  $z$  by mirrors. Lenses  $L_1$  and  $L_2$ , see Fig. 2(a), consist of two identical microscope objectives ( $4\times$ ,  $\text{NA} = 0.1$ , entrance pupil diameter  $R = 4.42$  mm), radius of  $I_1$  and  $I_2$  are  $R_1 = 1$  mm and  $R_2 = 0.75$  mm. This gives  $w = 0.61\lambda/(0.1R_1/R) = 17$   $\mu\text{m}$ . Imaging of the sources is made by lens  $L_3$  with focal length  $f_3 = 30$  cm. The input circular polarization is ensured by the polarizer and quarter-wave plate whereas the contra-circularly polarized field component after the optical vortex mask OVM is selected by another set of quarter-wave plate and polarizer (not shown in Fig. 2). Finally, all images are recorded by 12-bit room-temperature camera.

The coronagraphic behavior of our self-engineered spin-orbit masks is illustrated in Figs. 2(b) and 2(c) that show the so-called ‘rings of fire’ surrounding a dark area with diameter  $2R_1f_2/f_1$  (hence  $2R_1$  in our case) in the exit pupil plane  $P_2$ . The four-fold rotational symmetry for  $m = -1$  is reminiscent of the elastic anisotropy of the liquid crystal. Indeed, while only twist distortions are involved for  $m = +1$  when  $K_2 < K_1$ , both chiral and splay distortions at play for  $m = -1$  [24] break the axisymmetry, see [27] for recent numerical investigations. Ensuing starlight rejection is demonstrated in Figs. 3(a) and 3(b) that refer to the image of the on-axis source is collected in the plane  $P_3$  when the coronagraph is ‘on’ (i.e., presence of Lyot stop  $I_2$ ) or ‘off’ (i.e.,  $I_2$  is removed) while azimuth-averaged radial intensity profiles in the plane  $P_2$  are shown as solid curves in Fig. 3(c). More quantitatively, the coronagraph performances are gauged by evaluating the rejection of on-axis illumination. A peak-to-peak starlight rejection ratio of  $\mathcal{R}_{\text{peak, exp}} \approx 1000$  is obtained and is associated with typical power rejection rate  $\mathcal{R}_{\text{power, exp}} \approx 50$  defined as the ratio between the

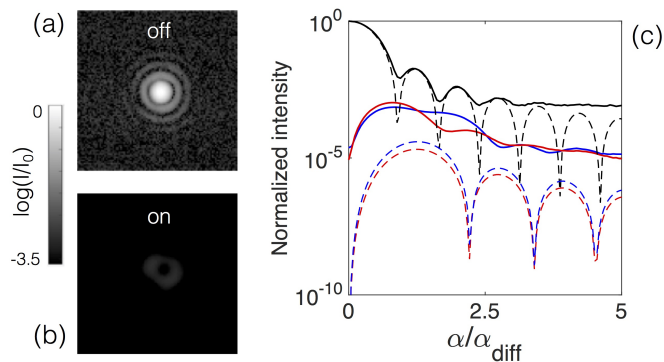


FIG. 3: (a,b) Typical on-axis point-like source images in the plane  $P_3$  when the coronagraph is off/on, with  $I_0$  is the maximal intensity in the off state while the intensity range refers to the 4096 camera levels. (c) Azimuth-averaged angular intensity distribution in on (black curves) and off (color curves) states. Solid curves: experimental data; dashed curves: simulations; red curves:  $m = +1$ ; blue curves:  $m = -1$ .

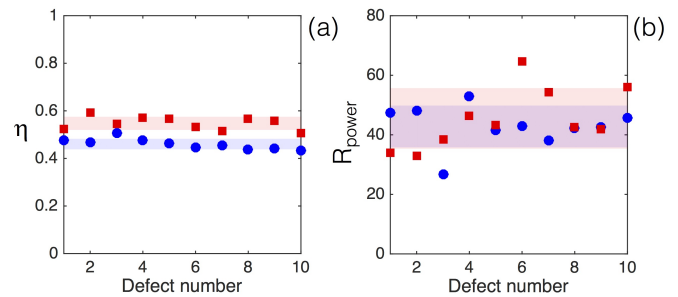


FIG. 4: Spin-orbit masks performances statistics. (a) Purity  $\eta$  of the optical vortex generation process. (b) Power rejection rate  $\mathcal{R}_{\text{power}}$ . Colored area refer to standard deviation region. Red square markers:  $m = +1$ ; blue circle markers:  $m = -1$ .

power outside and inside the Lyot stop,

$$\mathcal{R}_{\text{power}} = \int_{R_2}^{\infty} I_2(r) r dr / \int_0^{R_2} I_2(r) r dr. \quad (4)$$

where  $I_2(r)$  is the intensity profile in the exit pupil plane  $P_2$ . Statistical data from ten defects for  $m = \pm 1$  is summarized in Fig. 4. The purity  $\eta$  shown in Fig. 4(a) is evaluated as the ratio between the power of the generated vortex beam (post-selection circular polarizer is present) and the total output power (post-selection circular polarizer is removed). Experimental data is  $\eta_{\text{exp}} \simeq (0.55 \pm 0.02, 0.46 \pm 0.02)$  for  $m = \pm 1$ . On the other hand, statistics of measured power rejection rates are shown in Fig. 4(b) that gives  $\mathcal{R}_{\text{power, exp}} \simeq (46 \pm 9, 43 \pm 7)$  for  $m = \pm 1$ .

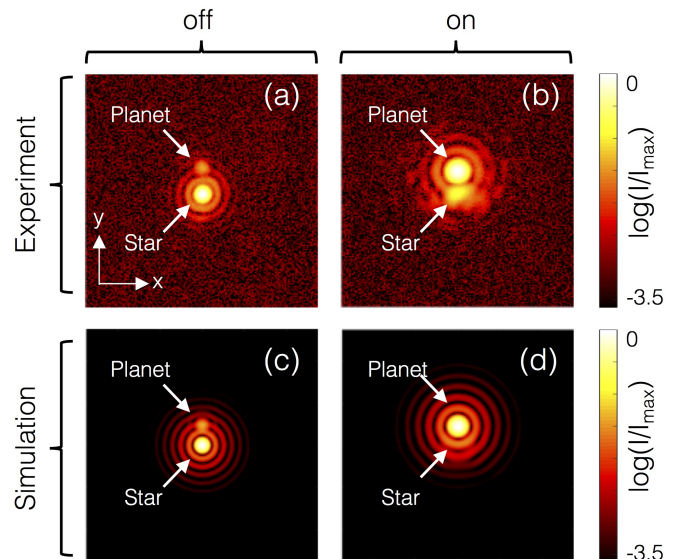


FIG. 5: Imaging a star/planet system when the coronagraph is off (without the Lyot stop, which gives smaller point spread function than the case when iris  $I_2$  is present) and on. (a,b) Experimental data. (c,d) Simulations.  $I_{\text{max}}$  is the maximal intensity of each image.

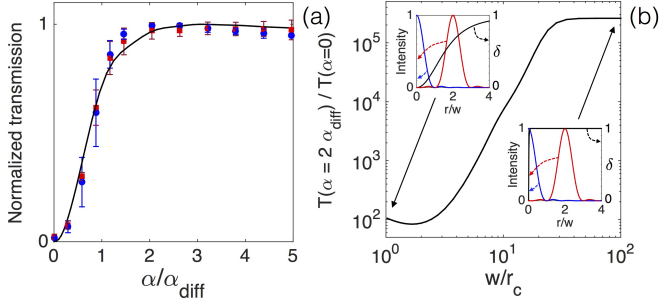


FIG. 6: (a) Coronagraphic throughput evaluated from the transmitted power ratio  $P_{\text{on}}/P_{\text{off}}$  as a function of the normalized angular separation distance  $\alpha/\alpha_{\text{diff}}$  to the telescope axis for  $m = \pm 1$ . Markers: experimental data with red/blue color for  $m = \pm 1$ . Solid curves: simulations. (b) Calculated ratio  $T(2\alpha_{\text{diff}})/T(0)$ . Insets: normalized intensity profiles of on-axis ( $\alpha = 0$ ) and off-axis ( $\alpha = 2\alpha_{\text{diff}}$ ) point sources and  $\delta$  in the vortex mask plane  $P_F$  for  $w/r_c = 1$  and  $w/r_c = 100$ .

Comparison of experimental data to the model is done under the assumption of a paraxial on-axis plane wave impinging on the iris  $I_1$ , namely by considering  $E_1 \propto \text{circ}(r/R_1)$  as the entrance pupil field in the plane  $P_1$ , where  $\text{circ}(r/\rho) = 0$  for  $r > \rho$  and  $\text{circ}(r/\rho) = 1$  for  $r < \rho$ . Then,  $\eta$  is calculated by inserting the expression of starlight intensity profile in the plane  $P_F$ , namely  $I_F = |\mathcal{F}[E_1]|^2$ , in Eq. (2) where  $\mathcal{F}$  refers the Fourier transform. This gives  $\eta_{\text{model}} = (0.80, 0.75)$  for  $m = \pm 1$ . On the other hand  $I_2(r) = |\mathcal{F}^{-1}[\tau(r, \phi)\mathcal{F}[E_1]]|^2$ , where  $\mathcal{F}^{-1}$  refers the Fourier transform, gives  $\mathcal{R}_{\text{peak, model}} \simeq (5 \times 10^4, 2 \times 10^4)$  for  $m = \pm 1$ . Finally, inserting the latter expression of  $I_2(r)$  in Eq. (4) gives  $\mathcal{R}_{\text{power, model}} \approx (3000, 1500)$  for  $m = \pm 1$ . Unsurprisingly, the model predicts better performances, indeed any source of imperfection is not taken into account (e.g., non-axisymmetry of defect at large scale, non-ideal polarization filtering).

Next we implement the coronagraphic observation of a ‘star/planet’ system. This is done by adding a faint off-axis illumination (the ‘planet’) at an angle  $2\alpha_{\text{diff}}$  ( $\alpha_{\text{diff}} = 0.61\lambda/R_1$  is the diffraction limit) from the on-axis light (the ‘star’) obtained from a distinct laser source. The experimental situation without coronagraph is shown in Fig. 5(a) where the peak-to-peak intensity ratio between star and planet in the imaging plane  $P_3$  is  $I_{\text{star}}/I_{\text{planet}} = 20$  for the purpose of demonstration. The latter ratio is drastically reduced down to 0.15 when the vortex mask is electrically turned on, see Fig. 5(b). Data is compared with simulations taking the same conditions as in experiments. Namely, the images of star and planet are calculated from  $I_j = |\mathcal{F}[E_j]|^2$  when the coronagraph is off (Lyot stop is removed) and  $I_j = |\mathcal{F}[\text{circ}(r/R_2)\mathcal{F}^{-1}[\tau(r, \phi)\mathcal{F}[E_j]]]|^2$  when the coronagraph is on, with  $E_{\text{star}} = \sqrt{20}\text{circ}(r/R_1)$  and  $E_{\text{planet}} = \text{circ}(r/R_1)\exp(i2k\alpha_{\text{diff}}y)$ ,  $k = 2\pi/\lambda$ . More quantitatively, the coronagraphic throughput is experimentally

assessed from the transmitted power ratio  $P_{\text{on}}/P_{\text{off}}$  of the light field passing through the Lyot stop when coronagraph is on and off as a function of  $\alpha/\alpha_{\text{diff}}$ . Fig. 6(a) summarizes data obtained for three independent defects for each  $m$ , where markers refer to experiment while solid curve corresponds to simulations, which exhibit good agreement. Moreover, the central apodization effect of the spin-orbit vortex mask due to the  $r$ -dependent retardance profile (Fig. 1(a)) is illustrated in Fig. 6(b) that shows the ratio  $T(2\alpha_{\text{diff}})/T(0)$  between the transmission of two identical off-axis ( $\alpha = 2\alpha_{\text{diff}}$ ) and on-axis ( $\alpha = 0$ ) point sources as a function of the ratio  $w/r_c$  when the coronagraph is on, taking  $\Delta_{\infty} = \pi$ ,  $R_1 = 1$  mm and  $R_2 = 0.75R_1$  whatever  $r_c$ . Apodization drawback manifests typically for  $w < 10r_c$  whereas for  $w > 10r_c$  the asymptotic high-contrast regime is reached. The cut-off ratio for  $w/r_c$  of course decreases with the separation between the sources. Finally, we note that present self-engineered liquid crystal spin-orbit vortex masks are not restricted to operate at a predetermined central wavelength since  $\Delta_{\infty}$  is electrically tunable as is the case of their artificial self-engineered counterparts [28].

More broadly, the proposed Nature-assisted technological approach to the fabrication of singular phase masks for optical imaging applications goes beyond possible use in optical vortex coronagraphy as demonstrated here and also includes stimulated emission depletion microscopy [29] and spiral phase contrast microscopy [30]. Moreover, the proposed approach is not restricted to pure phase masks and opens the way to self-engineered apodization masks that are heavily used in coronagraphy [31], which may involve the use of either transparent or absorbing liquid crystal mesophases. Further work is of course needed, in particular regarding large vortex mask size issues as usually requested in low numerical aperture telescopes, however it is likely that vortex masks endowed with both temporal and spatial reconfiguration capabilities may find attractive applications.

## FUNDING INFORMATION

This study has been carried out with financial support from the French State, managed by the French National Research Agency (ANR) in the frame of the Investments for the future Programme IdEx Bordeaux LAPHIA (ANR-10-IDEX-03-02).

- 
- [1] M. Mayor and D. Queloz, *Nature* **378**, 355–359 (1995).
  - [2] B. Lyot, *Mon. Not. R. Astron. Soc.* **99**, 580–594 (1939).
  - [3] F. Roddier and C. Roddier, *Publ. Astron. Soc. Pac.* **109**, 815–820 (1997).
  - [4] R. Soummer, K. Dohlen, and C. Aime, *Astron. Astrophys.* **403**, 369–381 (2003).
  - [5] D. Rouan, P. Riaud, A. Boccaletti, Y. Clenet, and A. Labeyrie, *Publ. Astron. Soc. Pac.* **112**, 1479–1486 (2000).
  - [6] D. Mawet, P. Riaud, O. Absil, and J. Surdej, *Astrophys. J.* **633**, 1191–1200 (2005).
  - [7] G. Foo, D. M. Palacios, and G. A. Swartzlander, *Opt. Lett.* **30**, 3308–3310 (2005).
  - [8] G. A. Swartzlander, *J. Opt. A: Pure Appl. Opt.* **11**, 094022 (2009).
  - [9] G. Biener, A. Niv, V. Kleiner, and E. Hasman, *Opt. Lett.* **27**, 1875–1877 (2002).
  - [10] L. Marrucci, C. Manzo, and D. Paparo, *Phys. Rev. Lett.* **96**, 163905 (2006).
  - [11] D. Mawet, E. Serabyn, K. Liewer, C. Hanot, S. McEldowney, D. Shemo, and N. E. O’Brien, *Opt. Express* **17**, 1902–1918 (2009).
  - [12] N. Murakami, S. Hamaguchi, M. Sakamoto, R. Fukumoto, A. Ise, K. Oka, N. Baba, and M. Tamura, *Opt. Express* **21**, 7400–7410 (2013).
  - [13] S. C. McEldowney, D. M. Shemo, R. A. Chipman, and P. K. Smith, *Opt. Lett.* **33**, 134–136 (2008).
  - [14] D. Mawet, E. Serabyn, K. Liewer, K. Burruss, J. Hickey, and D. Shemo, *Astrophys. J.* **709**, 53–57 (2010).
  - [15] S. R. Nersisyan, N. V. Tabiryan, D. Mawet, and E. Serabyn, *Opt. Express* **21**, 8205–8213 (2013).
  - [16] C. Delacroix and et al., *Proc. of SPIE* **9147**, 91478Y (2014).
  - [17] E. Brasselet, N. Murazawa, H. Misawa, and S. Juodkazis, *Phys. Rev. Lett.* **103**, 103903 (2009).
  - [18] C. Loussert, U. Delabre, and E. Brasselet, *Phys. Rev. Lett.* **111**, 037802 (2013).
  - [19] E. Brasselet, *Phys. Rev. A* **82**, 063836 (2010).
  - [20] E. Brasselet and C. Loussert, *Opt. Lett.* **36**, 719–720 (2011).
  - [21] R. Barboza, U. Bortolozzo, G. Assanto, E. Vidal-Henriquez, M. G. Clerc, and S. Residori, *Phys. Rev. Lett.* **109**, 143901 (2012).
  - [22] B. Yang and E. Brasselet, *J. Opt.* **15**, 044021 (2013).
  - [23] B. Son, S. Kim, Y. H. Kim, K. Kalantar, H.-M. Kim, H.-S. Jeong, S. Q. Choi, J. Shin, H.-T. Jung, and Y.-H. Lee, *Opt. Express* **22**, 4699–4704 (2014).
  - [24] A. Rapini, *J. Phys.* **34**, 629–633 (1973).
  - [25] E. Brasselet, *Opt. Lett.* **38**, 3890 (2013). In that paper, the misprint “*q integer*” should be replaced by “*q half-integer*”.
  - [26] P. Oswald and P. Pieransky, *Nematic and cholesteric liquid crystals: Concepts and physical properties illustrated by experiments* (Taylor & Francis, CRC, Boca Raton, FL, 2005).
  - [27] M. G. Clerc, E. Vidal-Henriquez, J. D. Davila, and M. Kowalczyk, *Phys. Rev. E* **90**, 012507 (2014).
  - [28] S. Shlussarenko, A. Murauski, T. Du, V. Chigrinov, L. Marrucci, and E. Santamato, *Optics Express* **19**, 4085 (2011).
  - [29] S. W. Hell and J. Wichmann, *Opt. Lett.* **19**, 780–782 (1994).
  - [30] S. Furhapter, A. Jesacher, S. Bernet, and M. Ritsch-Marte, *Opt. Express* **13**, 689–694 (2005).
  - [31] A. Carlotti, L. Pueyo, and D. Mawet, *Astron. Astrophys.* **566**, A31 (2014).

- 
- [1] M. Mayor and D. Queloz, “A jupiter-mass companion to a solar-type star,” *Nature* **378**, 355–359 (1995).
- [2] B. Lyot, “A study of the solar corona and prominences without eclipses,” *Mon. Not. R. Astron. Soc.* **99**, 580–594 (1939).
- [3] F. Roddier and C. Roddier, “Stellar coronagraph with phase mask,” *Publ. Astron. Soc. Pac.* **109**, 815–820 (1997).
- [4] R. Soummer, K. Dohlen, and C. Aime, “Achromatic dual-zone phase mask stellar coronagraph,” *Astron. Astrophys.* **403**, 369–381 (2003).
- [5] D. Rouan, P. Riaud, A. Boccaletti, Y. Clenet, and A. Labeyrie, “The four-quadrant phase-mask coronagraph. i. principle,” *Publ. Astron. Soc. Pac.* **112**, 1479–1486 (2000).
- [6] D. Mawet, P. Riaud, O. Absil, and J. Surdej, “Annular groove phase mask coronagraph,” *Astrophys. J.* **633**, 1191–1200 (2005).
- [7] G. Foo, D. M. Palacios, and G. A. Swartzlander, “Optical vortex coronagraph,” *Opt. Lett.* **30**, 3308–3310 (2005).
- [8] G. A. Swartzlander, “The optical vortex coronagraph,” *J. Opt. A: Pure Appl. Opt.* **11**, 094022 (2009).
- [9] G. Biener, A. Niv, V. Kleiner, and E. Hasman, “Formation of helical beams by use of pancharatnam-berry phase optical elements,” *Opt. Lett.* **27**, 1875–1877 (2002).
- [10] L. Marrucci, C. Manzo, and D. Paparo, “Optical spin-to-orbital angular momentum conversion in inhomogeneous anisotropic media,” *Phys. Rev. Lett.* **96**, 163905 (2006).
- [11] D. Mawet, E. Serabyn, K. Liewer, C. Hanot, S. McEldowney, D. Shemo, and N. E. O’Brien, “Optical vectorial vortex coronagraphs using liquid crystal polymers: theory, manufacturing and laboratory demonstration,” *Opt. Express* **17**, 1902–1918 (2009).
- [12] N. Murakami, S. Hamaguchi, M. Sakamoto, R. Fukumoto, A. Ise, K. Oka, N. Baba, and M. Tamura, “Design and laboratory demonstration of an achromatic vector vortex coronagraph,” *Opt. Express* **21**, 7400–7410 (2013).
- [13] S. C. McEldowney, D. M. Shemo, R. A. Chipman, and P. K. Smith, “Creating vortex retarders using photoaligned liquid crystal polymers,” *Opt. Lett.* **33**, 134–136 (2008).
- [14] D. Mawet, E. Serabyn, K. Liewer, K. Burruss, J. Hickey, and D. Shemo, “The vector vortex coronagraph: Laboratory results and first light at palomar observatory,” *Astrophys. J.* **709**, 53–57 (2010).
- [15] S. R. Nersisyan, N. V. Tabiryan, D. Mawet, and E. Serabyn, “Improving vector vortex waveplates for high-contrast coronagraphy,” *Opt. Express* **21**, 8205–8213 (2013).
- [16] C. Delacroix and et al., “Development of a subwavelength grating vortex coronagraph of topological charge 4,” *Proc. of SPIE* **9147**, 91478Y (2014).
- [17] E. Brasselet, N. Murazawa, H. Misawa, and S. Juodkazis, “Optical vortices from liquid crystal droplets,” *Phys. Rev. Lett.* **103**, 103903 (2009).
- [18] C. Loussert, U. Delabre, and E. Brasselet, “Manipulating the orbital angular momentum of light at the micron scale with nematic disclinations in a liquid crystal film,” *Phys. Rev. Lett.* **111**, 037802 (2013).
- [19] E. Brasselet, “Spin-orbit optical cross-phase-modulation,” *Phys. Rev. A* **82**, 063836 (2010).
- [20] E. Brasselet and C. Loussert, “Electrically controlled topological defects in liquid crystals as tunable spin-orbit encoders for photons,” *Opt. Lett.* **36**, 719–720 (2011).
- [21] R. Barboza, U. Bortolozzo, G. Assanto, E. Vidal-Henriquez, M. G. Clerc, and S. Residori, “Vortex induction via anisotropy stabilized light-matter interaction,” *Phys. Rev. Lett.* **109**, 143901 (2012).
- [22] B. Yang and E. Brasselet, “Arbitrary vortex arrays realized from optical winding of frustrated chiral liquid crystals,” *J. Opt.* **15**, 044021 (2013).
- [23] B. Son, S. Kim, Y. H. Kim, K. Kalantar, H.-M. Kim, H.-S. Jeong, S. Q. Choi, J. Shin, H.-T. Jung, and Y.-H. Lee, “Optical vortex arrays from smectic liquid crystals,” *Opt. Express* **22**, 4699–4704 (2014).
- [24] A. Rapini, “Umbilics : Static properties and shear-induced displacements,” *J. Phys.* **34**, 629–633 (1973).
- [25] E. Brasselet, “Optical angular momentum conversion in a nanoslit: comment,” *Opt. Lett.* **38**, 3890 (2013). In that paper, the misprint “ $q$  integer” should be replaced by “ $q$  half-integer”.
- [26] P. Oswald and P. Pieransky, *Nematic and cholesteric liquid crystals: Concepts and physical properties illustrated by experiments* (Taylor & Francis, CRC, Boca Raton, FL, 2005).
- [27] M. G. Clerc, E. Vidal-Henriquez, J. D. Davila, and M. Kowalczyk, “Symmetry breaking of nematic umbilical defects through an amplitude equation,” *Phys. Rev. E* **90**, 012507 (2014).
- [28] S. Slussarenko, A. Murauski, T. Du, V. Chigrinov, L. Marrucci, and E. Santamato, “Tunable liquid crystal q-plates with arbitrary topological charge,” *Optics Express* **19**, 4085 (2011).
- [29] S. W. Hell and J. Wichmann, “Breaking the diffraction resolution limit by stimulated emission: stimulated-emission-depletion fluorescence microscopy,” *Opt. Lett.* **19**, 780–782 (1994).
- [30] S. Furrer, A. Jesacher, S. Bernet, and M. Ritsch-Marte, “Spiral phase contrast imaging in microscopy,” *Opt. Express* **13**, 689–694 (2005).
- [31] A. Carlotti, L. Pueyo, and D. Mawet, “Apodized phase mask coronagraphs for arbitrary apertures ii. comprehensive review of solutions for the vortex coronagraph,” *Astron. Astrophys.* **566**, A31 (2014).